Original Article

Institution of MECHANICAL ENGINEERS
Journal of MECHANICAL ENGINEERING SCIENCE

Proc IMechE Part C:
J Mechanical Engineering Science
2018, Vol. 232(3) 457–465

DOI: 10.1177/0954406217742941
journals.sagepub.com/home/pic
SAGE

Effects of initial conditions on the coalescence of micro-bubbles

Rou Chen, Huidan(Whitney) Yu and Likun Zhu

Abstract

The effects of initial conditions on the coalescence of two equal-sized air micro-bubbles (R_0) in water are studied using the lattice Boltzmann method. The focus is on effects of two initial set-ups of parent bubbles, separated by a small distance d and connected with a neck bridge radius r_0, on the neck bridge growth at the early stage of the bubble coalescence. A sophisticated free energy lattice Boltzmann method model based on the Cahn-Hilliard diffuse interface approach is employed. This lattice Boltzmann method model has been demonstrated suitable for handling a large density ratio of two fluids up to 1000 and capable of minimizing the nonphysical spurious current. In both initial scenarios, the neck bridge evolution exhibits a half power-law scaling, $r/R_0 = A_0(t/t_i)^{1/2}$ after a development time. The half power-law agrees with the recent analytical prediction and experimental results. It has been found that smaller initial separation distance or smaller initial neck bridge radius results in faster growth of neck bridge and bubble coalescence, which is similar to the effects of these two initial scenarios on droplet coalescence. The physical mechanism behind each behavior has been explored. For the initial connected case, faster neck growth and longer development time corresponding to smaller initial neck radius is due to the significant bias between the capillary forces contributed by the meniscus curvature and the neck bridge curvature, whereas in the case of initial separated scenario, faster growth and shorter development time corresponding to shorter separation distance is due to the formation of elongated neck bridge. The prefactor A_0 that represents the growth of neck bridge radius at the characteristic time t_i captured in each case is in good agreement with the experimental results.

Keywords

Lattice Boltzmann method, bubble coalescence, neck bridge evolution, initial neck radius, initial separated distance

Date received: 30 July 2017; accepted: 25 October 2017

Introduction

Coalescence is a common process in gas–liquid systems. When two bubbles/droplets are close, a microscopic connecting neck bridge will form and rapidly grow tending to merge and minimize the surface area. Studying the neck bridge (contact area) growth at the early stage of coalescence is essential in understanding the dynamics of bubble/droplet coalescence.[1–5] Many efforts have been focused on the neck bridge evolution of droplet coalescence through numerical,[6–8] experimental[9,10] and theoretical[11] studies. The general understanding is that the neck bridge growth is governed by both resisting force (inertial force and viscous force) and driving force (capillarity force) characterized by Ohnesorge number (viscous force versus inertial and capillarity forces), $Oh(\equiv \eta_h/\sqrt{\rho_h \sigma L})$ where L, η, ρ, σ are the characteristic length, e.g. droplet/bubble radius R_0, viscosity, density, and surface tension respectively. The subscript h means the heavier fluid. For example, if viscous effect is negligible (i.e. $Oh \ll 1$), the coalescence of two identical droplets with radius R_0 is dominated by inertial force with a coalescence timescale $t_i = \sqrt{\rho_h R_0^3/\sigma}$ (i.e. in the inertial regime).[10] In this regime, neck bridge evolution has been analytically,[11,12] experimentally,[13] and numerically[6] studied. The time evolution of the neck bridge radius r (defined in Figure 1(b)) follows a power-law, $r/R_0 \propto (t/t_i)^{1/2}$, in the early stage of coalescence. When viscous force becomes significant (i.e. $Oh > 1$), the coalescence timescale is determined by $t_v = \mu R_0/\sigma$ (i.e. in the viscous regime). Neck bridge evolution is found to be $r/R_0 \propto t/t_v ln(t/t_v)$.[11] Paulsen et al.[14] analytically predicted that the neck bridge evolution of bubble coalescence follows the same half power-law scaling, i.e. $r/R_0 \propto (t/t_c)^{1/2}$, in the inertial and viscous regimes

Mechanical Engineering Department, Indiana University-Purdue University, Indianapolis (IUPUI), Indianapolis, IN, USA

Corresponding author:
Huidan(Whitney) Yu, Mechanical Engineering Department, Indiana University Purdue University at Indianapolis, Indianapolis, IN, USA.
Email: whyu@iupui.edu

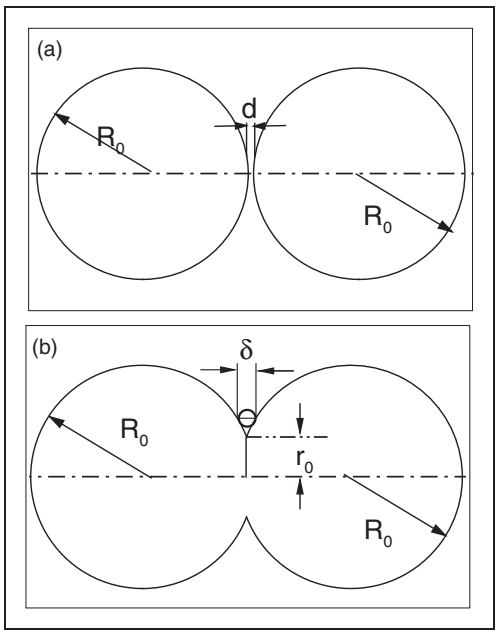

Figure 1. Schematics of two initial scenarios for two equal bubbles with radius R_0: (a) separated bubbles with distance d and (b) connected bubbles with neck bridge radius r_0 and meniscus diameter δ. The meniscus curvature is $K_d = 2/d$.

where the characteristic time t_c corresponds to t_i and t_v, respectively. This prediction was confirmed by experiment results.[14]

Separated with small distance d or connected with a small neck bridge radius r_0, schematized in Figure 1(a) and (b) respectively, are two typical initial set-ups in the research of bubble/droplet coalescence. In scenario (a), when the distance d is small enough, two bubbles/droplets are attracted through Van de Waals attraction force till bubbles/droplets touch when the coalescence starts.[15,16] Whereas in scenario (b), the initial radius r_0, corresponding to a meniscus diameter δ thus meniscus curvature $K_\delta = 2/\delta$, is usually due to small perturbation because the static touch of two bubbles/droplets is not stable and the coalescence starts immediately. The effects of these two scenarios on droplet coalescence have been studied numerically.[4] It has been observed that for scenario (a), the bridge evolution is sensitive to the distance of the initial separation, and for scenario (b), a slower initial growth corresponds to a larger initial neck bridge radius. The dynamics of microbubble coalescence under various influences are systematically investigated. Recently, the effects of size inequality of bubbles on the interfacial dynamics and coalescence time had been found that the coalescence time exhibits power-law scaling to the size inequality of parents bubbles[17] has already been studied. The present work is a part of continuous research effort on the aforementioned subject.

The early stage of air (light fluid with subscript l) microbubble coalescence in water (heavy fluid with subscript h) is studied using lattice Boltzmann method (LBM)[18,19] under two initial conditions. The focus is on how the initial setup of two bubbles affects the early neck bridge evolution. These are numerical evidence of the aforementioned half power-law scaling.[14] The kinetic-based LBM has emerged as an alternative for simulating a broad class of complex flows.[20,21] In the past three decades, several multiphase models using LBM have been developed, including the color fluid model,[22] the pseudo-potential model,[23] the mean-field model,[24] the phase-field model[25] based on the free-energy theory,[26] and the entropic LBM.[27] These methods have been continuously refined and applied to simulate many multiphase flow problems, (see general LBM reviews[20,21] and specific multiphase LBM reviews,[28,29] and therein references). The free-energy modeling approach is employed that has been continuously developed and refined in the last 10 years by Lee group[30–33] and it has been claimed that the parasitic current has been eliminated[32] and large density gradient is up to 1000[31] across the interface.

The remainder of the paper is organized as follows: the Lattice Boltzmann method for gas-liquid flows at high-density ratio section describes the free-energy LBM modeling and computational setup. Numerical results are shown in the Numerical simulation and results section, including validation through power-law scaling and initial condition effects on the neck bridge evolution at the early stage as well as the exploration of the mechanism. The paper concludes with the Summary and discussion section.

Lattice Boltzmann method for gas–liquid flows at high-density ratio

The present work is a part of continuous effort to explore the underlying mechanisms of the coalescence of microbubbles. The detail formulation of the LBM can be found in Chen et al.[17] The related equations are listed as follow.

Governing equations

For a binary flow, the governing equations including Cahn-Hilliard equation, pressure evolution equation and momentum equation are as follow

$$\partial C/\partial t + \mathbf{u}\cdot\nabla C = \nabla\cdot(M\nabla\mu) \tag{1}$$

$$\partial p_1/\partial t + \rho c_s^2 \nabla\cdot\mathbf{u} = 0 \tag{2}$$

$$\rho(\partial\mathbf{u}/\partial t + \mathbf{u}\cdot\nabla\mathbf{u}) = -\nabla p_1 + \mu\nabla C + \nabla\cdot\eta(\nabla\mathbf{u} + (\nabla\mathbf{u})^T) \tag{3}$$

where C is composition, μ is the chemical potential defined as

$$\mu = \mu_0 - \kappa\nabla^2 C \tag{4}$$

with $\mu_0 (= \partial E_0/\partial C)$ the classical part of the chemical potential. In this case, assume that the energy E_0 takes

the following form[34] of $E_0 = \beta C^2(C-1)^2$ with β being a constant. As a result, $\mu_0 = \partial E_0/\partial C = 2\beta C(C-1)(2C-1))$. In an interface at equilibrium, the interface profile of C is

$$C(z) = 0.5 + 0.5\tanh(2z/D) \tag{5}$$

where z is the distance normal to the interface and D is the (numerical) interface thickness, which is chosen based on accuracy and stability. Given D and β, one can compute the gradient parameter $\kappa = \beta D^2/8$ and the surface tension force $\sigma = \sqrt{2\kappa\beta}/6$.

The intermolecular force[32] is introduced as $\mathbf{F} = (1/3)\nabla\rho c^2 - \nabla p_1 - C\nabla\mu$ where p_1 is the hydrodynamic pressure, whereas the thermodynamic pressure p_0 is defined by $p_0 = \mu_0 - E_0 = \beta C^2(C-1)(3C-1)$. The total pressure is $p = p_0 + p_1 - \kappa C\nabla^2 C + \kappa|\nabla C|^2/2$. When Ma is low, $p_1/p_0 \sim O(Ma^2)$, and all thermodynamic quantities are independent of the hydrodynamic pressure.[35]

Lattice Boltzmann equations for binary flow

Targeting to the numerical stability and elimination of the spurious current caused by intermolecular force, Lee and Lin[30,31] adopted a new transformation technique, and then Lee continuously refined it based on Cahn-Hilliard diffusion scheme to eliminate the spurious current due to incompressibility.[32,33]

A new particle distribution function is defined as $g_\alpha = f_\alpha c^2/3 + (p_1 - \rho c^2/3)\Gamma_\alpha(0)$, in which $\Gamma_\alpha(\mathbf{u}) = \omega_\alpha[1 + 3(\mathbf{e}_\alpha\cdot\mathbf{u})/c^2 + 9(\mathbf{e}_\alpha\cdot\mathbf{u})^2/2c^4 - 3\mathbf{u}^2/2c^2]$. Here ω_α is the weight coefficient, e_α is the discretized velocity, and $c = dx/dt = 1$ in lattice units (i.e.,$\delta t = \delta x = 1$). Taking the total derivative $D_t = \partial_t + \mathbf{e}_\alpha\cdot\nabla$ of g_α results in

$$\begin{aligned}\partial g_\alpha/\partial t + \mathbf{e}_\alpha\cdot\nabla g_\alpha &= -(g_\alpha - g_\alpha^{eq})/\tau \\ &+ (\mathbf{e}_\alpha - \mathbf{u})\cdot[(1/3)\nabla\rho c^2(\Gamma_\alpha - \Gamma_\alpha(0)) - C\nabla\mu\Gamma_\alpha]\end{aligned} \tag{6}$$

where the new equilibrium $g_\alpha^{eq} = \omega_\alpha[p_1 + \rho((\mathbf{e}\cdot\mathbf{u}) + 3(\mathbf{e}_\alpha\cdot\mathbf{u})^2/2c^2 - u^2)]$. Discretizing equation (6) along characteristics over the time step δt, the LBE for g_α is

$$\begin{aligned}\bar{g}_\alpha(\mathbf{x} + \mathbf{e}_\alpha\delta t, t + \delta t) =& \bar{g}_\alpha(\mathbf{x}, t) - \frac{1}{\tau + 0.5}(\bar{g}_\alpha - \bar{g}_\alpha^{eq})|_{(\mathbf{x},t)} \\ &+ (\mathbf{e}_\alpha - \mathbf{u})\cdot[(1/3)\delta t\nabla^{MD}\rho c^2(\Gamma_\alpha(\mathbf{u}) \\ &- \Gamma_\alpha(0)) - C\delta t\nabla^{MD}\mu\Gamma_\alpha]|_{(\mathbf{x},t)}\end{aligned} \tag{7}$$

where ∇^{MD} means mixed difference approximation, and ∇^{CD} means central difference approximation[33] and the non-dimensional relaxation time $\tau = 3\nu/\delta t$, in which ν is the kinematic viscosity. In equation (7), the modified particle distribution function $\bar{g}_\alpha$ and the equilibrium distribution function $\bar{g}_\alpha^{eq}$ are introduced to facilitate computation

$$\begin{aligned}\bar{g}_\alpha = g_\alpha + [1/(2\tau)](g_\alpha - g_\alpha^{eq}) - (1/2)\delta t(\mathbf{e}_\alpha - \mathbf{u}) \\ \cdot[(1/3)\nabla^{CD}\rho c^2(\Gamma_\alpha(\mathbf{u}) - \Gamma_\alpha(0)) - C\nabla^{CD}\mu\Gamma_\alpha]\end{aligned} \tag{8}$$

$$\begin{aligned}\bar{g}_\alpha^{eq} = g_\alpha^{eq} - (1/2)\delta t(\mathbf{e}_\alpha - \mathbf{u})\cdot[(1/3)\nabla^{CD}\rho c^2 \\ (\Gamma_\alpha(\mathbf{u}) - \Gamma_\alpha(0)) - C\nabla^{CD}\mu\Gamma_\alpha]\end{aligned} \tag{9}$$

The hydrodynamic pressure and momentum can be computed by taking the zeroth and first moments of $\bar{g}_\alpha$.

$$p_1 = \sum\bar{g}_\alpha + (\delta t/6)\mathbf{u}\cdot\nabla^{CD}\rho c^2 \tag{10}$$

$$\rho u = (3/c^2)\sum\mathbf{e}_\alpha\bar{g}_\alpha - (\delta t/2)C\nabla^{CD}\mu \tag{11}$$

For the transformation of the composition C, a second distribution function is introduced in a simple format of $h_\alpha = (C/\rho)f_\alpha$ and $h_\alpha^{eq} = (C/\rho)f_\alpha^{eq}$. Similarly, taking the total derivative D_t of h_α and utilizing equation (1) yield

$$\begin{aligned}\bar{h}_\alpha(\mathbf{x} + \mathbf{e}_\alpha\delta t,\ t + \delta t) = \bar{h}_\alpha(\mathbf{x},\ t) &- \frac{(\bar{h}_\alpha - \bar{h}_\alpha^{eq})|_{(\mathbf{x},\ t)}}{\tau + 0.5} \\ &+ \delta t(\mathbf{e}_\alpha - \mathbf{u})\cdot[\nabla^{MD}C \\ &- \frac{3C}{\rho c^2}(\nabla^{MD}p + C\nabla^{MD}\mu)]\ \Gamma_\alpha|_{(\mathbf{x},\ t)} \\ &+ \delta tM\nabla^2\mu\ \ \Gamma_\alpha|_{(\mathbf{x},\ t)}\end{aligned} \tag{12}$$

and the modified particle distribution function $\bar{h}_\alpha$ and $\bar{h}_\alpha^{eq}$ is defined as[33]

$$\begin{aligned}\bar{h}_\alpha = h_\alpha + \frac{1}{2\tau}(h_\alpha - h_\alpha^{eq}) - \frac{\delta t}{2}(\mathbf{e}_\alpha - \mathbf{u}) \\ \cdot\left[\nabla^{CD}C - \frac{3C}{\rho c^2}(\nabla^{CD}p + C\nabla^{CD}\mu)\right]\Gamma_\alpha\end{aligned} \tag{13}$$

$$\bar{h}_\alpha^{eq} = h_\alpha^{eq} - \frac{\delta t}{2}(\mathbf{e}_\alpha - \mathbf{u})\cdot[\nabla^{CD}C - \frac{3C}{\rho c^2}(\nabla^{CD}p + C\nabla^{CD}\mu)]\Gamma_\alpha \tag{14}$$

The composition C can be computed by taking the zeroth moment of $\bar{h}_\alpha$

$$C = \sum\bar{h}_\alpha + 0.5\delta tM\nabla^2\mu \tag{15}$$

The density ρ and the dimensionless relaxation frequency $(1/\tau)$ are taken as linear functions of the composition by

$$\rho(C) = C\rho_1 + (1-C)\rho_2, \quad 1/\tau(C) = C/\tau_1 + (1-C)/\tau_2 \tag{16}$$

As discussed in Lee,[32] the interfacial mobility M in equation (15) plays a role in suppressing the non-physical parasitic currents caused by the numerical discretization. In the present study, $M(=6.67)$ is set as suggested.

While the formation of LBEs above seems complicated, the implementation of them is straightforward as follows.

Parameters in lattice unit. ρ_h, ρ_l, σ, $D=4$, $\beta=12\sigma/D$, $\kappa=3/2\sigma D$, $M=6.67$, τ_h, τ_l.

Initial conditions. $p_1=0$, $\mathbf{u}_i=0$, C, ρ, τ, μ, h^{eq}, and g^{eq} are calculated by equations (5), (16), (16), (4), (14), and (9) respectively.

Iteration

1. Collision: the right-hand sides of equations (12) and (7), respectively.
2. Streaming: the left-hand sides of equations (12) and (7), respectively.
3. Variable update: C, ρ, τ, $\rho\mathbf{u}$, p_1, h^{eq}, and g^{eq} by equations (15), (16), (16), (11), (10), (14), and (9) correspondingly.

Numerical simulation and results

The early-stage coalescence ($t<5\,\mu$s) of two identical air micro-bubbles are studied, $R_0(=20\ \mu$m) sitting at the center of a square domain filled with water. The side length of the domain is 100 μm. For the purpose of exploring the effects of initial conditions of the bubbles on the bubble coalescence, two conditions are considered, as schematized in Figure 1. In case (a), the bubbles are separated by a distance d. It is known[15,36,37] that when the separation of two bubbles is within the effective range of intermolecular attraction force, the attraction force will drive the bubbles moving toward. When the bubbles are touched, a bridge is formed and then the bubble coalescence starts. Figure 2 shows the instantaneous velocity vector fields right before and right after the neck bridge forms. Small separation distance is selected to ensure the occurrence of coalescence. The ratio of separation distance and bubble radius, $\gamma_d(\equiv d/R_0)$, varies from 0.008 to 0.042. In case (b), the bubbles are connected with an initial neck bridge radius r_0 which is taken by initial perturbation to propagate.[4,6,9] The ratio of initial bridge neck radius and bubble radius $\gamma_r(\equiv r_0/R_0)$ changes from 0.16 to 0.38. The domain boundaries in vertical and horizontal directions are periodic. The density and viscosity of the water and air are $\rho_h=10^3(\mathrm{kg/m^3})$, $\rho_l=1.2(\mathrm{kg/m^3})$ and $\eta_h=10^{-3}\mathrm{kg/(ms)}$, $\eta_l=1.98\times10^{-5}\mathrm{kg/(ms)}$, respectively, resulting in the density ratio 833 and viscosity ratio 50.5 of water vs. air. The surface tension between water and air is assumed to be $\sigma=7.2\times10^{-2}N/m$. Such a physical setup was used

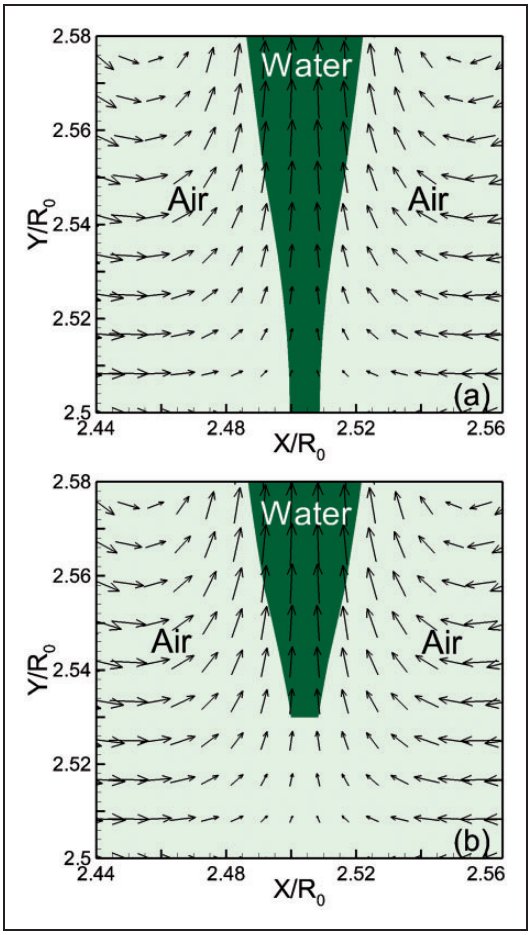

Figure 2. Instantaneous velocity fields right before (a) and right after (b) two bubbles are connected forming a neck bridge.

in the entire study unless otherwise indicated. D2Q9 lattice model[19] is applied in the simulation.

First, convergence check through the power-law scaling of neck bridge evolution is performed to find out an appropriate resolution. Selecting $\gamma_d=0.017$ and $Oh=2.6\times10^{-2}$ (inertial regime) and varying five spatial resolutions of $200^2, 400^2, 600^2, 800^2, 1000^2$ for the flow domain. It is found that in all the five cases, the time evolution of neck bridge radius r follows power-law $r/R_0=A_0(t/t_i)^{1/2}$, in which $t_i=\sqrt{\rho_h R_0^3/\sigma}=10.5\,\mu$s, and t is measured from the instant of bubble coalescence, with varying A_0, as shown in Table 1. The neck bridge radius r is determined through a contour line of $C=0.4$. As the resolution increases, A_0 converges to 1.06 with reducing relative errors. To avoid high computation cost, 600^2 is selected as the typical resolution to produce the results for the present study. The half power-law scaling, $r/R_0\propto(t/t_i)^{1/2}$, meets the analytical prediction.[14] The prefactor $A_0=1.05$ for this resolution is within the range of experimental measurements[1,38] 1.09 ± 0.08, for air bubbles coalescence in water.

Table 1. Resolution convergence check.

Resolution	200^2	400^2	600^2	800^2	1000^2
A_0	0.9181	1.1017	1.050	1.056	1.060
Relative error	13.39%	4.06%	0.94%	0.37%	0

Note: The relative error is for the finest resolution.

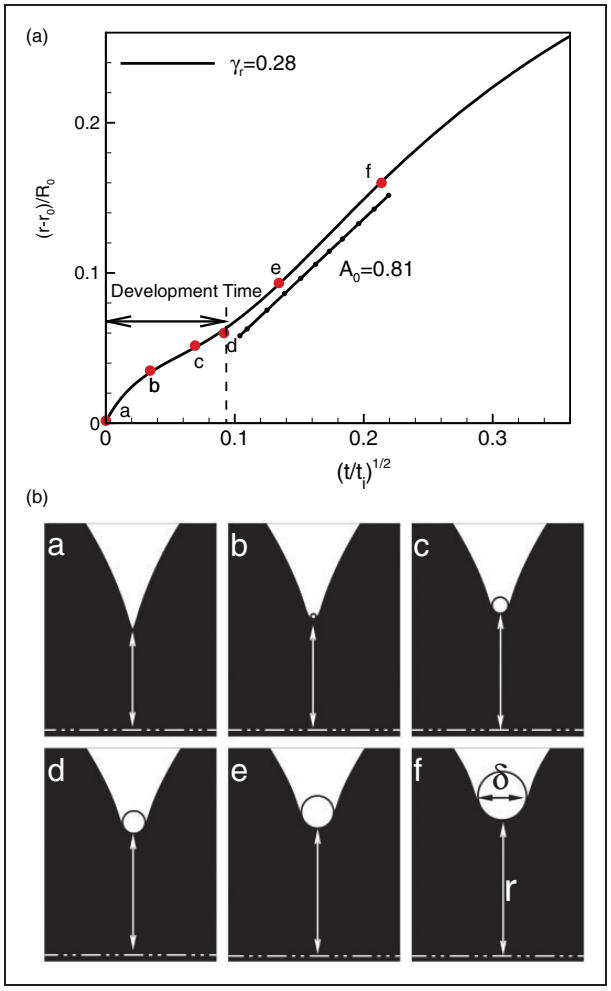

Figure 3. (a) A representative neck bridge evolution for the case of $g_r = 0.28$. (b) Sequence of meniscus development and neck growth across development time (from a to d) and half power-law scaling time (from d to f).

Effects of initial neck bridge radius r_0 on neck bridge evolution

In this section, five cases with the relative radii of the initial neck bridge, $\gamma_r(= r_0/R) = 0.16, 0.20, 0.28, 0.33,$ and 0.38, are investigated. Figure 3 shows the neck bridge evolution of a representative case ($\gamma_r = 0.28$). It can be seen in Figure 3(a) that after a development time, the relative growth of neck bridge, $(r - r_0)/R_0$, becomes linear to $(t/t_i)^{1/2}$, which is equivalent to the half power-law of $(r - r_0)/R_0 = 0.81(t/t_i)^{1/2}$. The half power-law scaling has been predicted analytically,[11] which has been confirmed in recent experiments.[14] The result is a numerical confirmation of the half power-law scaling. In order to understand the underlying physics of the early neck growth, the driving mechanism to the coalescence in this early stage is closely looked into. Figure 3(b) shows the neck bridge development in the development time from a to d and half power-law scaling regime from d to f indicated in Figure 3(a). As the neck bridge radius r increases gradually, pushing the bottom of the neck up, the meniscus gradually rounds up with increased diameter δ. Table 2 lists the curvature of meniscus ($K_\delta = 2/\delta$) vs. curvature of neck bridge ($K_r = 1/r$) at the corresponding time sequence. At initial time (point a), the neck bridge radius is set to be small and corresponds a steep meniscus, resulting in the curvature of the meniscus 5600 times larger than the curvature of the neck bridge. This implies that the initial growth of the neck bridge is driven by the curvature of the meniscus within a very short time period ($0.01t_i$) from point a to d, the meniscus curvature K_δ rapidly reduces by 29311% from 1000.0 to 3.4 μm^{-1} while the neck curvature K_r only reduces around 21% from 0.179 to 0.147 μm^{-1}, toward a more balanced driving mechanism contributed by both meniscus curvature and neck bridge curvature. In the time period of half power-law scaling from time point d to f, it is seen that the ratio of the two curvatures is around 15. Thus, the time development before the half-power law scaling is due to the significantly unbalanced capillary force of the meniscus curvature and the neck curvature.

Table 2. Curvature of meniscus (K_δ) vs. curvature of neck bridge (K_r) at representative time points indicated in Figure 3(a).

Time Point	δ	r	$K_\delta(= 2/\delta)$	$K_r = (1/r)$	K_δ/K_r
A	0.002	5.6	1000.0	0.179	5600
b	0.067	6.3	29.9	0.159	188
c	0.417	6.6	4.8	0.152	32
d	0.583	6.8	3.4	0.147	23
e	0.833	7.1	2.4	0.141	17
f	1.250	7.6	1.6	0.132	12

Note: Units: δ and r (μm). K_δ and K_r (μm^{-1}).

The time evolutions of the neck bridge with different initial neck bridge radius are plotted in Figure 3, distinguished by the dimensionless parameter $\gamma_r(= r_0/R_0)$. The solid line corresponds to the representative case discussed above. While each initial radius case has a similar tendency of the neck growth to the representative case, it is seen that smaller γ_r (from bottom up) results in faster growth of the neck bridge, meaning that smaller initial neck bridge leads to faster coalescence at the early stage. It is noticed that the plotted power-law scaling is

$(r - r_0)/R_0 = A_0(t/t_i)^{1/2}$ for the purpose to compare different initial neck bridge radius r_0. Meanwhile, smaller γ_r exhibits faster neck bridge evolution. This is understandable. Smaller γ_r corresponds to larger initial curvature of meniscus, resulting in large capillary force to drive the neck growth, leading to faster coalescence. Corresponding to the smallest $\gamma_r = 0.16$ (long-dash line), the initial curvature of meniscus and neck bridge is as high as 2985 as opposed to 1000 of the representative case (solid line). These effects of initial neck bridge radius on micro-bubble coalescence are similar to those on droplet coalescence.[4]

Effects of initial separation distance (d) on neck bridge evolution

In this part, five cases with different initial separation distance d, distinguished by $\gamma_d (= d/R_0) =$ 0.008, 0.017, 0.025, 0.033, 0.042, are investigated. The time evolutions of the neck bridge are plotted in Figure 5. Once again, the half power-law scaling after a development time is seen in each separation case, which is another numerical confirmation for the analytical prediction.[11] It is seen that smaller separation distance (bottom up) leads to faster neck growth, thus faster coalescence, and shorter development time. Table 3 lists the development time for each case. The smallest γ_d case starts the half power-law almost immediately when two bubbles attach. Whereas the largest γ_d case takes $0.289t_i$ before starting the half power-law. The development time for this initial scenario is the result of elongated neck formation, as explored in a study of the effects of initial separation distance to the neck growth in droplet coalescence.[4] As the initial separation d is small enough, within the effective range of the intermolecular attraction force, the attraction force between the two approaching surfaces initiates the thinning and rupture of the liquid film between two bubbles and forms a gas bridge. The film thinning leads to an elongated neck bridge in the horizontal direction. As seen in Figure 6 for two initial separation distance cases with $\gamma = 0.008$ (a) and 0.042 (b), respectively, smaller separation distance forms shorter neck bridge with larger curvature of meniscus. The larger meniscus curvature leads to faster neck growth thus faster coalescence, as have been discussed above.

The prefactor A_0 represents the relative neck bridge radius r/R_0 at $t = t_i$. Table 3 shows that for the

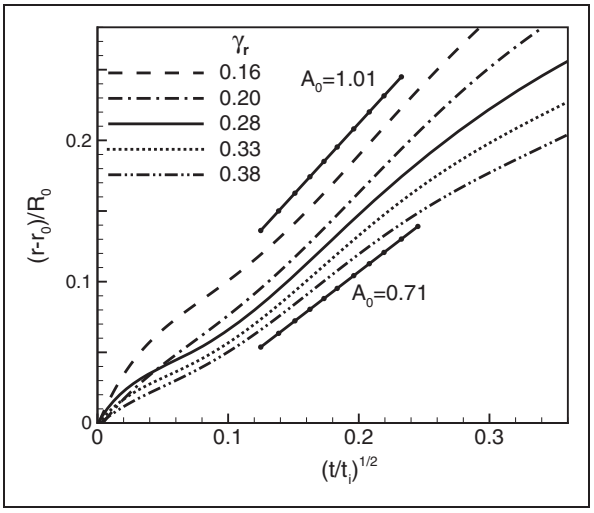

Figure 4. Effects of initial neck bridge radius ($r_r = r_0/R_0$) on the growth of the neck bridge radius (r/R_0). The solid line corresponds to the representative case in Figure 3.

Table 3. Effect of γ_d on the development time.

γ_d	0.008	0.017	0.025	0.033	0.042
Development Time (t/t_i)	0	0.0076	0.0196	0.0256	0.289
A_0	1.05	1.08	1.12	1.12	1.13

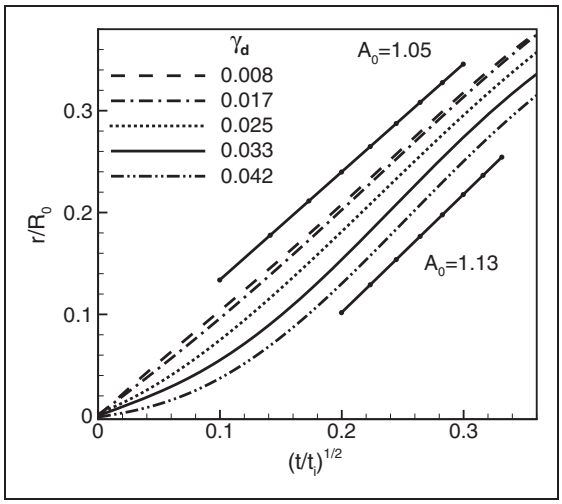

Figure 5. Effects of initial separation distance ($r_d = d/R_0$) on the growth of the neck bridge radius (r/R_0).

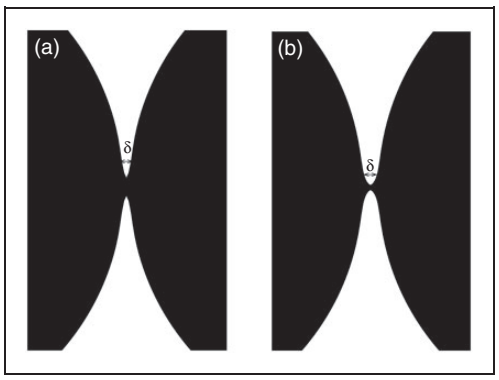

Figure 6. Effects of initial separation distance on the formation of elongated neck bridge in horizontal direction, (a) $r_d = 0.008$ and (b) $r_d = 0.042$.

Table 4. Table list of prefactor A_0 from literature.

A_0	$\rho_h(\mathrm{kg/m^3})$	$\eta(\mathrm{N \cdot s/m^2})$	$\sigma(\mathrm{N/m^2})$	$R_0(\mathrm{mm})$
1.24[1]	931	5.0×10^{-3}	0.020	2.0
1.11[1]	750	2.0×10^{-2}	0.020	2.0
1.14[1]	1000	1.0×10^{-3}	0.073	2.0
1.29 ± 0.05[38]	792	5.9×10^{-4}	0.023	1.94
1.09 ± 0.08[38]	1000	1.0×10^{-3}	0.073	1.94
1.03 ± 0.07[38]	1160	1.44×10^{-2}	0.067	1.94

varying initial separation distance cases, A_0 varies marginally from 1.05 to 1.13. This is in good agreement with the experimental results. Table 4 shows A_0 values of different liquids. The experimental cases are all in the inertial regime, the same as the present study. It seems that A_0 is closely related to the density of liquid. Larger liquid density results in smaller A_0. The current work studies air bubble coalescence in water with the liquid density of $\rho_h = 1000\,\mathrm{kg/m^3}$. The range of A_0 in the present work agrees well with the experimental results.

Summary and discussion

In this paper, the effects of two initial set-ups, i.e. separated and connected bubbles, have been studied respectively, on the neck bridge evolution using the LBM. To insure the reliability of the results, convergence check and validation have been carefully performed. Simulation results show that the two initial conditions have significant influence on the neck growth thus the coalescence dynamics. In both initial scenarios, the neck bridge evolution exhibits half power-law scaling, $r/R_0 = A_0(t/t_i)^{1/2}$ after a development time. The half power-law agrees with the recent analytical prediction and experimental results. It has been found that small initial separation distance or small initial neck bridge radius results in faster growth of neck bridge and bubble coalescence, which is similar to the effects of these two initial scenarios on droplet coalescence. The physical mechanism behind the development time is explored. For the initial connected case, smaller neck bridge radius corresponds to steeper meniscus at the liquid side, leading to significantly larger curvature of meniscus than that of neck bridge. The development time is to lessen the significant bias and enable contributions from both curvatures of meniscus and neck bridge to capillary forces. Whereas for the initial separated case, the thinning of liquid film between two bubbles causes elongated neck bridge in the approaching direction of two bubbles due to intermolecular attraction. In the range of intermolecular attraction, smaller separation distance leads to a steeper meniscus (equivalent to larger curvature or larger capillary force). This explains why smaller separation distance shows faster neck growth. Meanwhile, smaller separation distance forms smaller elongated neck bridge and thus causes shorter development time to start the half power-law scaling. The values of the prefactor A_0 in the power-law scaling for all the cases are in good agreement with the experimental results. These simulation results are expected to provide informative guidance for initial set-up of numerical simulation of bubble coalescence.

Declaration of Conflicting Interests

The author(s) declared no potential conflicts of interest with respect to the research, authorship, and/or publication of this article.

Funding

The author(s) disclosed receipt of the following financial support for the research, authorship, and/or publication of this article: This research was supported by the National Science Foundation (grant no. 1264739). And this work used the Extreme Science and Engineering Discovery Environment (XSEDE), which was supported by National Science Foundation (grant no. ACI-1053575).

References

1. Aarts D, Lekkerkerker H, Guo H, et al. Hydrodynamics of droplet coalescence. *Phys Rev Lett* 2005; 95: 164503.
2. Thoroddsen S, Etoh T, Takehara K, et al. On the coalescence speed of bubbles. *Phys Fluid (1994-present)* 2005; 17: 071703.
3. Bremond N, Doméjean H and Bibette J. Propagation of drop coalescence in a two-dimensional emulsion: a route towards phase inversion. *Phys Rev Lett* 2011; 106: 214502.
4. Baroudi L, Kawaji M and Lee T. Effects of initial conditions on the simulation of inertial coalescence of two drops. *Comput Math Appl* 2014; 67: 282–289.
5. Munro J, Anthony C, Basaran O, et al. Thin-sheet flow between coalescing bubbles. *J Fluid Mech* 2015; 773: R3-1-R3-12.
6. Duchemin L, Eggers J and Josserand C. Inviscid coalescence of drops. *J Fluid Mech* 2003; 487: 167–178.
7. Sprittles J and Shikhmurzaev Y. Coalescence of liquid drops: Different models versus experiment. *Phys Fluids* 2012; 24: 122105.
8. Sprittles J and Shikhmurzaev Y. A parametric study of the coalescence of liquid drops in a viscous gas. *J Fluid Mech* 2014; 753: 279–306.
9. Menchaca-Rocha A, Martínez-Dávalos A, Nunez R, et al. Coalescence of liquid drops by surface tension. *Phys Rev E* 2001; 63: 046309.
10. Kavehpour H. Coalescence of drops. *Ann Rev Fluid Mech* 2015; 47: 245–268.
11. Eggers J, Lister J and Stone H. Coalescence of liquid drops. *J Fluid Mech* 1999; 401: 293–310.
12. Charles G and Mason S. The coalescence of liquid drops with flat liquid/liquid interfaces. *J Colloid Sci* 1960; 15: 236–267.
13. Aryafar H and Kavehpour H. Drop coalescence through planar surfaces. *Phys Fluids (1994-present)* 2006; 18: 072105.
14. Paulsen J, Carmigniani R, Kannan A, et al. Coalescence of bubbles and drops in an outer fluid. *Nat Commun* 2014; 5: 3182–3199.

15. Ivan U, Vakarelskia U, Manicad R, et al. Dynamic interactions between microbubbles in water. *PNAS* 2010; 107: 11177–11182.
16. Firouzi M, Howes T and Nguyen A. A quantitative review of the transition salt concentration for inhibiting bubble coalescence. *Adv Colloid Interf Sci* 2015; 222: 305–318.
17. Chen R, Yu H, Zhu L, et al. Spatial and temporal scaling of unequal microbubble coalescence. *AIChE* 2017; 63: 1441–1450.
18. Chen H, Chen S and Matthaeus W. Recovery of the Navier–Stokes equations using lattice-gas Boltzmann method. *Phys Rev A* 1992; 45: R5339–R5342.
19. Qian Y, Dhumieres D and Lallemand P. Lattice Boltzmann model for Navier–Stokes equation. *Europhys Lett* 1992; 17: 479–484.
20. Chen S and Doolen G. Lattice Boltzmann method for fluid flows. *Ann Rev Fluid Mech* 1998; 30: 329–364.
21. Aidun C and Clausen J. Lattice-Boltzmann method for complex flows. *Ann Rev Fluid Mech* 2010; 42: 439–472.
22. Andrew K, Gunstensen K, Daniel H, et al. Lattice Boltzmann model of immiscible fluids. *Phys Rev A* 1991; 43: 4320–4327.
23. Shan X and Chen H. Lattice Boltzmann model for simulating flows with multiphases and components. *Phys Rev E* 1993; 47: 1815–1819.
24. He X, Shan X and Doolen G. Discrete Boltzmann equation model for nonideal gases. *Phys Rev E* 1998; 57: R13.
25. Swift M, Osborn W and Yeomans J. Lattice Boltzmann simulation of nonideal fluids. *Phys Rev Lett* 1995; 75: 830–833.
26. Cahn J and Hilliard J. Free energy of a nonuniform system. I. interfacial free energy. *J Chem Phys* 1958; 28: 258–266.
27. Mazloomi MA, Chikatamarla S and Karlin I. Entropic lattice Boltzmann method for multiphase flows. *Phys Rev Lett* 2015; 114: 174502.
28. Chen L, Qinjun Kang Q, Mua Y, et al. A critical review of the pseudopotential multiphase lattice Boltzmann model: methods and applications. *Int J Heat Mass Transf* 2014; 76: 210–236.
29. Connington K and Lee T. A review of spurious currents in the lattice boltzmann method for multiphase flows. *J Mech Sci Technol* 2012; 26: 3857–3863.
30. Lee T and Lin CL. A stable discretization of the lattice Boltzmann equation for simulation of incompressible two-phase flows at high density ratio. *J Comp Phys* 2005; 206: 16–47.
31. Lee T and Fischer P. Eliminating parasitic currents in the lattice Boltzmann equation method for nonideal gases. *Phys Rev E* 2006; 74: 046709.
32. Lee T. Effects of incompressibility on the elimination of parasitic currents in the lattice Boltzmann equation method for binary fluids. *Comput Math Appl* 2009; 58: 987–994.
33. Lee T and Liu L. Lattice Boltzmann simulations of micron-scale drop impact on dry surfaces. *J Comp Phys* 2010; 229: 8045–8063.
34. Jamet D, Lebaigue O, Coutris N, et al. The second gradient method for the direct numerical simulation of liquid–vapor flows with phase change. *J Comput Phys* 2001; 169: 624–651.
35. Day M and Bell J. Numerical simulation of laminar reacting flows with complex chemistry. *Combust Theory Model* 2000; 4: 535–556.
36. Chan D, Klaseboer E and Manica R. Film drainage and coalescence between deformable drops and bubbles. *Soft Matter* 2011; 7: 2235–2264.
37. Tabor R, Grieser F, Dagastine R, et al. Measurement and analysis of forces in bubble and droplet systems using AFM. *J Colloid Interface Sci* 2012; 371: 1–14.
38. Wu M, Cubaud T and Ho C. Scaling law in liquid drop coalescence driven by surface tension. *Phys Fluid* 2004; 16: L51–L54.

Appendix

Notation

A_0	prefactor of power-law scaling
c	lattice velocity in LBM
C	composition
d	separation distance
D	numerical interface thickness
e_α	discretized velocity in LBM
F	intermolecular force
g_α	particle distribution function which is used to recover momentum and pressure evolution equation
g_α^{eq}	equilibrium distribution function of g_α
$\bar{g}_\alpha$	modified particle distribution function of g_α
$\bar{g}_\alpha^{eq}$	modified equilibrium distribution function of g_α
h_α	particle distribution function which is used to recover Cahn-Hilliard evolution equation
h_α^{eq}	equilibrium distribution function of h_α
$\bar{h}_\alpha$	Modified particle distribution function of h_α
$\bar{h}_\alpha^{eq}$	modified equilibrium distribution function of h_α
K_δ	curvature of meniscus
K_r	curvature of neck bridge
L	characteristic length
M	mobility
Oh	Ohnesorge number
p	total pressure
p_0	thermodynamic pressure
p_1	dynamic pressure
r	neck bridge radius
r_0	initial neck bridge radius
R_0	bubble radius
t	time of neck bridge evolution
t_i	timescale in the inertial regime
t_v	timescale in the viscous regime
u	velocity of fluid
w_α	weight in the particle distribution function

β	constant in the classical part of the chemical potential
γ_d	the ratio of separation distance and bubble radius
γ_r	the ratio of initial neck bridge radius and bubble radius
Γ_β	particle distribution function
δ	diameter of meniscus
δt	time in lattice unit
δx	length in lattice unit
η	local dynamic viscosity
η_h	dynamic viscosity of heavy fluid
η_l	dynamic viscosity of light fluid
κ	gradient parameter
μ	chemical potential
μ_0	classical part of the chemical potential
ν	local kinematic visocity
ρ	local density
ρ_h	density of heavy fluid
ρ_l	density of light fluid
σ	surface tension
τ	non-dimensional relaxation time
∇^{CD}	central difference approximation
∇^{MD}	mixed difference approximation